Nano-engineered diamond-based materials for supercapacitor electrodes: A review

Katarzyna Siuzdak [a] and Robert Bogdanowicz [b*]

[a] *Centre for Plasma and Laser Engineering, The Szewalski Institute of Fluid-Flow Machinery, Polish Academy of Sciences, 14* Fiszera *St., 80-231 Gdansk, Poland*

[b] *Department of Metrology and Optoelectronics, Faculty of Electronics, Telecommunications and Informatics, Gdansk University of Technology, 11/12 G. Narutowicza St., 80-233 Gdansk, Poland*

***Corresponding author:** E-mail: ksiuzdak@imp.gda.pl (Katarzyna Sizudak); Tel.: +48-58-522 52 94; Fax: +48 58-341-61-44

Abstract

Owing to the popularity of carbon-based supercapacitors, diamond has also been examined as a potential candidate with unique advantages such as a wide electrochemical potential window and stable capacitive behavior in both aqueous and non-aqueous electrolytes. Moreover, its chemical stability in harsh environments at extreme applied potential and current provides rare opportunities for designing new supercapacitors. Owing to the intrinsic low surface area of diamond, it is necessary to increase the electrochemically active surface area or to produce diamond based composites ensuring capacitance improvement for the practical applications. According to the literature reports, the nano-engineered diamond structures can achieve a specific capacitance as high as 10 mF cm^{-2} with a specific energy of 10-100 Wh kg^{-1} in aqueous electrolyte. The present manuscript reviews the recent advancements in this topic of research by highlighting the potentials and challenges of diamond-based supercapacitors. The special attention was paid to fabrication methods and electrochemical performance of particular materials in view of further application for supercapacitor construction.

Keywords: Nanodiamonds, Porous diamond, Silicon nanowires, Boron-doped diamond; Diamond supercapacitors, electrochemical characterization

Introduction

Among various carbon nanomaterials examined for electric double layer capacitors (EDLCs) [1–3], diamond has also been considered because of its unique features [4–6]. Various diamond forms (thin layers, particles, foams) and phases as well as doping approach have been employed to achieve a high conductivity and developed surface area for the electrochemical performance. Figure 1 provides an overview of the different types of diamond-based supercapacitors reported in the literature as will be reviewed in the present manuscript. The chemical inactivity of diamond widens the stable electrochemical window, which is indeed a major advantage for supercapacitors. This in combination with the biocompatibility of diamond, has provided a different opportunity for employing the high electrochemical capacitance at neural interfaces, which is of medical interest [7].

Figure 1

Since pure diamond is recognizing as a perfect isolator, different impurities were introduced into its lattice, such as nitrogen or boron resulting in n- or p- type doping semiconducting behavior. Among different dopant atoms, boron is recognized as an excellent acceptor and relatively easily can be incorporated into the structure of diamond and diamond-like carbon (DLC) with energy level of 0.37 eV. As a source of dopant diborane (B_2H_6) could be used, realizing the process of synthesis in the standard mixture CH_4/H_2. B doping produces a material with many different conducting regions, and possibly different conducting pathways and mechanisms. With increasing boron concentration, a spread in the energy of the localized states of boron impurity centers induces the formation of an impurity band (with a band width of ~0.2 eV for a boron concentration of ~10^{19} cm^{-3}) and hopping conduction through nearest-neighbors or more distant impurities (variable range hopping) takes place. The conductivity is reduced and it could reach even level of mOhms per cm, but it happened just for heavily boron-doped films when concentrations exceeds 10^{21} cm^{-3}. The boron-doped diamond (BDD) films have been recognized as one of the best electrode materials offering excellent electrochemical performance [8], such as (i) a wide electrochemical potential window, (ii) low and stable capacitive currents in aqueous and non-aqueous solutions, (iii) weak or no surface bio-fouling, (iv) chemical resistance and stability in harsh environments and at high voltage/current densities [2]. Highly conductive BDD as a sp^3 carbon material may be then regarded as a promising capacitor electrode over other sp^2 carbon electrodes. Taking into account the boron concentration on the level of 10^{21} the potential windows of ca. 3.2 V in aqueous, 4.6 V in organic and even 4.9 V in ionic liquid based electrolytes are reached [9]. Knowing that specific capacity of stored energy is determined by a

simple equation ½CU^2, where C is specific capacitance and U states for cell voltage, the wide potential window offered by BDD significantly drive up its value.

Furthermore, the dangling bonds at the diamond surface can be terminated with hydrogen, hydroxyl or oxygen. This is similar to the structural irregularities of graphene enhancing the electrochemical activity[10]. The presence of different surface groups tunes the electronic properties of the solid/electrolyte interface along with the electrochemical interfacial state of the diamond surface and its double-layer properties, *e.g.*, wettability, the point of zero charge, adsorption of ions (capacitance) and self-discharge characteristics [1].

Since the typical CVD (chemical vapour deposition) diamond films are planar exhibiting low surface area, the majority of conducted studies are focused on the development of nano-engineered diamond structures with enhanced surface areas. Various approaches have been utilized to achieve diamond nanostructuring including selective top-down etching or bottom-up growth. The relevant fabrication methods for increasing the diamond surface area are listed in Figure 2 [11–14] .

Figure 2

There are four common approaches for the preparation of nanostructured diamond electrodes: (i) nanodiamond-based composites, (ii) porous CVD diamond, (iii) CVD diamond grown on Si nanowires, and (iv) CVD diamond composites. Each category is characterized by specific physicochemical properties, and thus, the features associated with the supercapacitor performance. The enhanced surface area of diamond jointly with its wide working potential windows (*ca*. 2.5 V in aqueous electrolytes and 7.3 V in organic electrolytes) make the thin material very promising for the fabrication of supercapacitors. Figure 3 displays the specific capacitance of numerous diamond based energy storage devices prepared by the aforementioned approaches.

Figure 3

It is worth noting that these approaches also modify the diamond molecular structure in addition to increasing the specific surface area. Reactive ion etching (RIE) of porous structures along with growth on silicon nanowires or TiO_2 nanotubes degenerates extraordinary parameters obtained in the planar diamond electrodes. The sp^2 phase enrichment, grain size reduction or mechanical deterioration (*e.g.*, cracks, film discontinuity) are commonly observed in the nanostructured diamond electrodes.

Nanodiamond based electrode materials

Nanodiamond (ND) soot can be fabricated in large scale by the detonation of carbon-containing explosives. Controlled oxidation process of ND by treatment by acid solution or oxygen-containing gaseous atmosphere ensures high sp^3 content. Application of ND recently grows up and also ND was proposed as a component of composite that is formed together with conducting polymer. Despite electroactive polymers are commonly utilized materials for supercapacitors, their performance could be improved by compositing with carbon nanomaterials for the practical applications[15]. In the case of ND, only its small amount embedded into the polymer matrix is needed to obtain composite with remarkably enhanced strength, toughness, elastic modulus, as well as thermal conductivity, specific heat capacity, and thermal stability comparing to the pure polymer. These improved properties are attributed to the "enhanced adhesion within the matrix," resulting in a better load transfer between the filler and the matrix [11].

Following these positive impact of ND presence, Kovalenko *et al*. demonstrated for the first time that low-cost detonation of ND powder could greatly enhance the performance of polyaniline (PANI) [16]. The incorporation of ND inside of PANI results in high surface area, decent mechanical properties, low cost and acceptable conductivity in the mean of energy storage applications, such as electrochemical capacitors. On the contrary to the pure polymer electrode, the specific capacitance of the PANI with embedded 3 wt. % of ND electrodes increases after 10,000 galvanostatic cycles and reaches a specific capacitance of 640 F g^{-1} in 1 M H_2SO_4 electrolyte (Figure 4). After multicyclic test, the specific capacitance of ND-PANI electrode is 2-3 times larger than that of polymer passed composite containing CNT or graphene and over 4 times higher than pure polymer material. Diamond nanoparticles introduced inside the PANI matrix are recognized as a toughening agent and thereby minimizing the volume changes within the polymer during charge/discharge cycles that extend electrode lifetime.

Figure 4

Similarly to Kvalenko, Zang *et al*. [17] proposed PANI-ND based electrode material obtained via the electropolymerization of PANI over the ND powder electrode. It was shown that polymer effectively links the ND particles, developing a porous structure resulting in a large specific surface area that could be useful in application as an electrode material in capacitors. The electrochemical impedance spectroscopy of that fabricated composite revealed an enhancement in the conductivity as compared with the pristine nanodiamond electrode.

The carbon nanoparticles could also be chemically modified to increase the specific capacitance, for example by using of phosphomolybdate[18]. However, comparing to onion like carbon or multiwall carbon nanotubes, such treatment of ND caused a significant reduction in its capacitance because of possible removal of the surface defects, edge planes or surface functional groups as proposed by Portet *et al.* [19]. Park *et al*. [18] attributed this phenomenon also to the significant differences of surface conductivities mainly depending on the sp^2/sp^3 ratio of the ND in comparison with the onion like carbon.

Other treatment of ND proposed also by Portet, concerns its vacuum annealing at above 1200°C and as a result carbon onion-like particles 5-15 nm in size are obtained. They showed a 35% increase of the surface area (500 ± 40 m^2 g^{-1}) as compared with the as-received ND. That effect is attributed to the particle densification and expansion during the thermally induced phase transformation towards graphitization as revealed by Raman spectroscopy and high-resolution transmission electron microscopy (TEM) [19]. It should be underlined, that finally OLC are utilized here as capacitance delivered material and ND soot was used only as a substrate for synthesis procedure.

Similarly to Portet, Sun *et al*. [20] used ND as an isolation component between graphene oxide (GO) sheets and then its annealing at 1200°C ensures graphitization and the onion like carbon formation. The specific area reached 420 m^2 g^{-1}r as a result of flexible mesoporous graphitic films prepared by thermal treatment with the use of GO sheets and ND particles. These electrodes exhibited high electrical conductivities in the range of 7.4 - 20 kS m^{-1}. The usage of ND allowed for OLCs incorporation within the GO 2D structure and further expansion of the graphitic interlayer resulting in an interlayer spacing of 0.79 nm (Figure 5A), which strengthens the chemical irregularities of the sp^2 carbons and enhances the electrochemical activity [10]. The porous GOC films were activated by immersing them in a mixed acidic solution (HNO_3: H_2SO_4) and investigated as a supercapacitor electrodes, where a specific capacitance of 143 F g^{-1} was obtained for the largest specific surface area composite (Figure 5B).

Figure 5

On the contrary to the high thermal treatment of nanodiamond particles, Wang *et al.* [21] proposed heating the ultrasonicated mixture with different content of reduced GO and ND only at 100°C for 48h. With a ratio of 10/1 within ND/rGO, the supercapacitor delivered a specific capacitance of 186 F g^{-1} determined in 1 M H_2SO_4 via galvanostatic discharge at 1 Ag^{-1} and 143 Fg^{-1} at $2Ag^{-1}$ Other approach elaborated by Wang *et al.* concerns addition of hydrazine to the obtained ND/rGO mixture during the synthesis procedure and resulting material delivers gravimetric capacitance of 241 Fg^{-1} .

The addition of reducing agent leads to most of oxygen-containing group removal and improved electrical properties were reached. Furthermore, the composite exhibit excellent long term stability tested upon 1,000 charge-discharge cycles.

To meet the demand of supercapacitors with high energy and power densities, the nanodiamond was used also together with ethyl cellulose and terminol to form a paste [22]. The electrode material formed via screen printing onto aluminum substrate plate following the two-step sintering at 300°C. Proposed preparation method was recognized as promising since ND exhibit high temperature and corrosion resistance.

Summarizing, the utilization of ND as an electrode component requires: i) thermal annealing that leads to OLC formation, ii) surface modification or iii) low-temperature annealing. Most of reported treatment procedures of ND are high energy consuming and unfortunately the electrical properties of ND are not competitive to those reported for other carbon materials as graphene or carbon nanotubes. The economical large-scale production of detonation NDs provided significant stimulus to technological applications. An overview of international patent applications in the field of nanodiamond concerning their quantity rapidly growing during the last few years[23]. European and US companies appear to be clearly reserved concerning both the utilization of nanodiamond-based materials and investments into appropriate R&D (approx. $200M in 2016). Whereas the NDs appear to be more promising in the areas of energy storage, environmental applications, composite materials, and nanotoxicity research.

Porous nanostructured diamond

As an alternative to the ultra-high thermal annealing inducing surface graphitization, the top-down approach was proposed as mentioned above. Nevertheless, that kind of processing methods, such as inductively coupled plasma etching cannot be scaled up simply and removal of the substantial fraction of diamond during etching procedure performed for flat diamond substrates, makes it commercially less attractive. Recently developed bottom-up processing allows to fabricate electrode materials within the matrix of porous template usually made from silica, zoolite or some biomaterials. After selective template removal, the remaining material is characterized with highly developed surface where large amount of charge could be accumulated.

Gao *et al*. [24] proposed to overgrow 0.5 μm silica spheres by CVD diamond followed by removal of the SiO_2 template in HF solution to fabricate diamond foam as displayed in Figure 6A. It is obvious that the specific capacitance of this electrode proportionally depends on the foam thickness. Since the

diamond foam was boron-doped, it could work over a wide potential window of 2.5 V in aqueous electrolyte. As above mentioned, heavy boron doping was realized due to ensure material p- type conductivity since pure diamond is a good electrical insulator.

Figure 6

The 2.6 μm thick boron-doped diamond foam results in an outstanding power density of 0.8 kW cm^{-3} and the energy density is comparable with that of the porous carbon-based micro-supercapacitors. Diamond foam electrode results in a capacitance of 0.598 mF cm^{-2} in an aqueous electrolyte and 0.436 mF cm^{-2} in an organic electrolyte (Figure 6B). At higher scan rates, this change turns is even more noticeable because of the larger size of the solvated ions and the lower dielectric constant of organic electrolytes.

The application of coral-like polypyrrole films as a basal material of porous boron-doped diamond electrode was reported by Hebert *et al*. [25]. The Raman spectrum of the porous BDD showed the broad signals at 480 and 1240 cm^{-1} as well as the down shift of the diamond peak at 1314 cm^{-1} indicating the high boron incorporation in the diamond film (approximately 10^{21} acceptors per cm^3). The diamond was grown at a temperature below 450 °C to limit the degradation of polypyrrole template. The polypyrrole/BDD electrodes display a wide potential window of about 2.8 V and capacitances of 3 mF cm^{-2} and 2.4 mF cm^{-2} were obtained in a $LiClO_4$ electrolyte for 90 and 190 nm thickness, respectively.

The nature-implied nanoporous honeycomb is another interesting approach for increasing the surface area of a planar diamond film. The porous structures have been developed by a Japanese group [26,27]. The honeycomb structures were fabricating from polished boron-doped diamond films by oxygen plasma etching through an anodic alumina mask resulting in *ca*. 60 nm pores over a large area of the surface (Figure 7A).

Figure 7

The capacitance of the honeycomb diamond depends mostly on the pore diameter. The 60 nm pore structure exhibited 1.97 mF cm^{-2} [26], while 400 nm pore-size film 3.91 mF cm^{-2} [27] because the capacitance is increased by increasing the roughness factor. This value varies with potential about 200 times larger than the prior as-grown diamond surface (Figure 7B). Interestingly, XPS studies

indicated the large concentration of oxygen on these films, but the electrodes showed a quite wide potential window of about 2.5 V (Figure 8A) [26]. The double-layer capacitive current recorded for the diamond honeycomb was 18 to 20 higher than that of the as-grown planar diamond electrode. Moreover, the potential window of honeycomb diamond is *ca*. 1.5 - 2.5 times wider than that obtained in the aqueous acid electrolyte (Figure 8A). As can be seen in Figure 8B, the charge/discharge profiles of the diamond-based electrodes are higher when compared with the activated carbon materials [27].

Figure 8

Kondo *et al*. [28] employed a thermal treatment to develop the porous, graphitized diamond due to the anisotropic etching effect depending on the crystal orientation and pore formation. Two-step thermal treatment: heating in argon at 1000 °C for pre-etching followed by heating in air at 425 °C for efficient graphitization. The etching is considered as a result of the exposure of the (111) faces, both for the original (111) and (100) facets. Etching occurs in the parallel direction in the former case, while reverse-pyramid and edges with rectangular textures are shaped in the latter as illustrated in Figure 9B.

Figure 9

This dense pores of tens to hundred nanometer sizes enhanced the voltammetric and galvanostatic performance resulting in a higher double-layer capacitance of up to 140 μF cm^{-2} [28], mainly due to the surface structure formed (Figure 9C,D). Comparable surface effects were obtained by Shi *et al*. [29], where boron doped diamond was selectively etched in hydrogen–argon plasma using Ni nanoparticles as a mask. This approach resulted in a higher capacitance of 9.55 mF cm^{-2} than that of thermally treated diamond [28]. This phenomenon is attributed to the high electrical conductivity and large specific surface area of nano-pores. The specific capacitance decreased to 98.2% of the initial capacitance after 500 cycles and then increased to 120.0% after10,000 cycles.

In a similar fashion, a sintered BDD electrode showed a capacitance of 4.19×10^{-6} to 5.11×10^{-6} F cm^{-2} depending on the electrolyte [30], and wet-chemical selective etching of the β-SiC/diamond composite [13] resulted in a porosity of 15 to 68% (Figure 2). Zhuang *et al*. [13] reported that the β-SiC/diamond composite had an excellent electrical conductivity a sheet resistance equal to 300 Ω sq^{-1}. Moreover, that approach displays outstanding double layer capacitance 17.3 F cm^{-2} at a scan rate of 100 mV s^{-1}. The porous diamond electrodes are potentials candidates not only for supercapacitors,

but also in other applications such as the water cleaning, catalyst−supports, and detoxification devices.

Chemical vapour deposited diamond composites

As it was stated above, the diamond electrodes include diamond honeycomb or aligned diamond nanowires characterized by enlarged surface area are promising materials for supercapacitors. These diamond nanostructures are fabricated based on top-down approaches using the diamond post-treatment, mainly via oxygen plasma-etching. However, the enlargement of the geometric surface is limited to *ca*. ten times because of permeability of the plasma and the duration of the mask etching. Additionally, loss of the diamond material during the top-down processing causes an increase in the fabrication cost. Therefore, alternative approaches might of practical interest. A possible method is to employ highly porous silicon substrates with an available large surface area for diamond growth.

Gao *et al*. [31] fabricated Si nanowires substrates using CVD via gold nanoparticles resulting in the formation of p-type Si wires with 50 nm in diameter and length of 5 μm. This process is accompanied by 13-times enlargement of the active surface in comparison with the planar Si substrate. In the next step, the ND seeding and then microwave CVD process in H_2/CH_4/trimethylborane mixture with B/C ratio of 4,000, were carried out. The sample (Figure 10A) consisted of Si nanowires covered by 135 nm-thin NCD layer, whereas Raman spectra proved the presence of highly boron doped diamond. The capacitive properties were tested in an ionic liquid (1-Methyl-1-propylpyrrolidinium bis(trifluoromethyl sulfonyl)imide, PMPyrrTFSI) in propylene carbonate (PC) that provided good conductivity and wettability. The capacitance was determined by cyclic voltammetry (CV) over a wide potential window of 4 V as shown in Figure 10B. At 1 V s^{-1}, the capacitance reaches 105 μF cm^{-2}, but drops to 47 μF cm^{-2} when increasing the scan rate to 100 V s^{-1}. The energy density was two orders of magnitude higher than that of the bare silicon. Furthermore, the supercapacitor retained 93.3% of its capacitance after 10 000 cycles at 5 V s^{-1}.

Figure 10

Aradilla *et al*. [32] fabricated Si nanowires via CVD process with a length of 50 μm with a diameter in the range of 20 - 200 nm, and a 100 nm-thick diamond coating was deposited (Figure 11A). The electrochemical performance was originated from the carbon-oxygen species and hydrogen on the surface adsorbed during the material doping and growth. The potential application was validated

during the tests of micro-supercapacitor (MSC) with a symmetric electrode arrangement performed at 10 mA cm^{-2} current density within 4 V cell voltage (–2.5– 1.5 V *vs*. Ag^{+}/Ag). As it is shown in Figure 11B, the areal capacitance reached 1.9 mF cm^{-2} at 2 mA cm^{-2} and dropped to 1.5 mF cm^{-2}. This value is fairly higher than those of EDL-MSC based on SiNWs (23-50 μF cm^{-2}), SiCNWs (120 μF cm^{-2}), SiC-coated SiNWs (850 μF cm^{-2}), multiwalled carbon nanotubes (200-400 μF cm^{-2}), diamond foams (300 μF cm^{-2}), and carbide-derived carbon (1.5 mF cm^{-2}). Electrochemical impedance spectroscopy (EIS) measurements suggested a relaxation time of 165 ms justifying the device ability to deliver high power densities in a very short time. The Ragone plot presented in Figure 11C indicates that MSC based on the BDD/SiNW electrode exhibits energy and power density values in the range of 11-15 mJ cm^{-2} and 3-25 mW cm^{-2}, respectively. The stability test performed over 1 million of galvanostatic charge/discharge cycles (GCD) showed 35%-decrease in the capacitance. The biggest drop is recorded during the first 50 000 cycles that are due to the oxidation of Si and carbon surface or the presence of impurities in the electrolyte. However, still, this device presents the best performance as compared with the CVD-grown SiNW-based MSC and morphology of electrode remains unchanged after prolonged GCD.

Figure 11

May and co-workers [33] reported a similar approach, but inductively coupled plasma (ICP) etching process of the Si substrate led to the formation of needles (SiN) reaching a length of almost 20 μm as shown in Figure 12A. The diamond coating was obtained via CVD process when diborane rich CH_4/H_2 mixture was used resulting in heavily boron-doped micro- or nanocrystalline diamond film over the Si needles (Figure 12B). The CV recorded for BDD/SiN material in an aqueous potassium nitrate solution (0.1 M) appear quasi-rectangular shape (Figure 12C) typical for the double-layer charging and significant difference in the capacitive current between different Si substrates covered by diamond is observed. The capacitance for partially overgrown BDD-coated Si long needles reaches 638 μF cm^{-2} whereas the flat BDD exhibits only 2.9 μF cm^{-2}, and BDD-coated short and long needles are characterized by an areal capacitance of 7.6 and 279.4 μF cm^{-2}, respectively. The increase in the double layer charge is ascribed to the large surface-area-to-volume-ratio rather to micro- or nano- crystalline diamond size. Therefore, the surface morphology plays more important role than differences in the grain size and sp^2 carbon content. Summarizing the usage of nanostructure Si substrate (wires, needles) for highly conductive diamond deposition allows reaching the high surface area and finally higher double layer capacitance being crucial for SC application.

Figure 12

Diamond based composites

The most effective approach for the enhancement of capacitive properties of diamond is compositing, where the diamond is permanently integrated with the other material, i.e. carbon fiber (CF) or nanotubes (CNT) as well as conducting polymer (CP) or metal oxide. Almeida *et al*. [34] formed a nanocrystalline diamond film over the carbon felt (10 μm in diameter) exhibiting superficial striated texture with small regions with deep groves. This morphology may increase the exposed surface for diamond nucleation, knowing that a highly distorted carbon gives better diamond nucleation than a flat surface. The CVD process was performed in an atmosphere of CH_4/H_2/Ar gas mixture. The material shown in Figure 13A was tested in 0.5 M H_2SO_4 via CV at different scan rates and the corresponding curves exhibit rectangular shape (Figure 13B). However, apart from the pseudocapacitance, the broad redox peaks arise due to a Faradaic process occurring on the material surface resulting from the presence of some functional groups.

Figure 13

The specific capacity equals 2.6 mF cm^{-2} for the carbon fiber produced at 1300 K. Similar works were carried on also in the case when the gas mixture was enriched by the boron source [35–37], resulting in the BDD coverage over the carbon fiber with the doping level of 1.5×10^{21} cm^{-3} [38]. The electrochemical performance revealed the strengthened capacitive behavior due to the increased surface area. The material BDD/CF thermally treated at 2000°C represented the largest area value, and thus, the highest current density is reached. Similarly, as it was in the case of non-doped diamond coated CF, the redox peaks appear on the CV curve and are attributed to some redox active groups, such as –OH or C=O. Additionally, EIS studies also indicated the lowest impedance value for the BDD/CF-2000, which is in consistent with the CV tests whereas the verification of the capacitance from the imaginary part gives 1.9 mF cm^{-2}. This value is explained in terms of the developed morphology, high roughness factor, and porosity since the amount of the electrical charge accumulated in the capacitor depends highly on the surface of the electrode/electrolyte interface and easy access of the charge carriers to this interface.

Carbon nanotubes have also been employed as substrates for the deposition of diamond. The first

work in this direction was done by Honda group [39] producing multiwall carbon nanotubes/nanoporous diamond composite electrode as presented in Figure 14A. The nanohoneycomb structure, achieved by oxygen plasma etching, was dedicated for both Li-ion battery and supercapacitor application.The measurements were performed in non-aqueous propylene carbonate solution containing: $LiClO_4$ and Et_4NBF_4. On the contrary to the as-deposited diamond, the CNT-modified showed the capability for the Li^+ intercalation/deintercalation (see Figure 14B). The highest discharge capacity was determined for the HD CNT-NANO and equals 408 mA cm^{-2}, while for the LD CNT-NANO sample, it reached only 112 mA cm^{-2} that is due to the reduced degree of void space in the nanopores facilitating the electrochemical access deep down the material. The electrochemical properties of the material were also studied in detail using EIS technique allowing to track the impedance of the Li^+ migration through the film, double-layer capacitance and reaction resistance for Li^+ intercalation. The charge/discharge tests showed that the average discharge capacity for LD CNT-NANO and HD-CNT-NANO is 117 and 43 mC cm^{-2}, respectively. Due to the suppression of the potential drop associated with Li^+ deintercalation by rapid charging/discharging from the electrical double-layer the increase of the specific power could be reached. Following that, proposed electrode material could be regarded as a suitable host material of for hybrid battery- and supercapacitor-like electrode, where CNT-deposited pores work as a Li^+ ion battery and the void pores of the nanodiamond surface that acting as a double-layer capacitor.

Figure 14

The research on carbon/diamond electrodes were also conducted in a typical aqueous electrolyte as it was reported by Zanin *et al*. [40,41]. The approach is based on: (i) formation of vertically aligned CNT (5 μm, 20-50 nm width) on the Si plate characterized by tepee (T) and honeycomb (H) shape of the surface morphology resulting in T-BDD and H-BDD composite materials and (ii) BDD deposition with the grain size of 1 μm. The SEM image of the material surface is presented in Figure 15A. Tepee and honeycomb structures were fabricated using vertically aligned carbon nanotubes (VACNT) with various lengths of 5 and 40 μm ion, respectively resulting in significant difference in areal density of the material CNT for further BDD deposit. On the contrary to T-BDD, as the substrate for H-BDD composite, the Ti plate was used that exhibits much higher conductivity comparing to a poorly semiconducting silicon. The CV scans performed in an aqueous solution of KNO_3 exhibits rectangular shape typical for double-layer charging but significant difference between flat BDD and BDD deposited onto T, or H-type CNW is observed (Figure 15A).

Figure 15

The highest currents and hence higher capacitance of the BDD/H-CNW electrode material are due to their higher real surface area, which also affects the CV shape in the presence of redox probes. The impedance studies performed at the formal potential of the redox reaction gives charge transfer resistance and space charge capacitance values that correspondingly 20-times decreases and 450-times grows up when the more expanded surface of the substrate for BDD deposition is used instead of the flat one. Other work focused on highly corrugated DLC films on the vertically aligned CNT (40 μm long, 60 nm in diameter) [41]. The Raman spectra for DLC:VACNT appears as a combination of the active modes, *i.e.*, typical for the DLC and carbon nanotubes. By cyclic voltammetry measurements performed in KNO_3, the areal capacitances of 875 and 642 μF cm^{-2} was estimated for the VACNT and DLC:VACNT at 0.15 V, respectively; which are fairy higher than typical double-capacitance values for the carbon electrode (5 μF cm^{-2}). The improvement in the capacitive current for vertically aligned CNT is attributed to the formation of oxygenated surface groups of the nanotubes that is unfortunately suppressed by the DLC coverage. The electroactive nature was also studied by EIS and a huge increase in the magnitude of the impedance amplitude |Z| of the DLC:VACNT and bare VACNT in comparison with the DLC film is observed. For DLC:VACNT, the conductivity over the whole surface was provided despite the insulating nature of the DLC grown on Si substrate. The capacitance from double layer formation of DLC:VACNT was estimated to be 45±3 μF with an electrode geometric surface area of 0.071 cm^2.

Another approach in the field of diamond-based composite electrodes is the possibility of utilizing conducting polymer. Tong *et al*. [42], deposited BDD film deposited onto a p-Si surface acting as the substrate for the electrochemical deposition of polyaniline with embedded multiwall carbon nanotube (MWCNT). The presence of the CNT provided large surface area and excellent electron transfer ability, and thus, resulted in a decrease of the charge transfer resistance and an increase of the double layer capacitance. Then, the bare PANI layer making this composite a promising candidate for supercapacitor application. Aradilla *et al*. [43] used silicon nanowires (50 μm-long; 20-200 nm in diameter) grown by CVD as the substrate, which was covered by diamond film, and finally poly(3,4-ethylenedioxythiophene) (PEDOT) layer. The electrochemical tests were carried out both in a three-electrode cell and for the symmetric micro-supercapacitor design using an ionic liquid solution of N1114TFSI (Butyltrimethylammonium bis(trifluoromethylsulfonyl)imide) as the electrolyte. The CV plots showed pseudocapacitive behavior associated with the polymer coating and the redox

couple corresponding to the reduction and oxidation reaction of PEDOT. The decrease in the specific capacitance from 140 F g^{-1} at 1 mV s^{-1} down to 24 F g^{-1} at 200 mV s^{-1} is observed, which is caused by the slow diffusion of the electrolyte ions at the high scan rate. The GCD studies performed at different current densities exhibited areal capacitance of 9.5 mF cm^{-2} at 0.1 mA cm^{-2}, which dropped to 8.5 mF cm^{-2} at 0.1 mA cm^{-2}, *i.e.*, similar to other SiNWs based heterojunctions with PEDOT (8 mF cm^{-2}), PPy (14 mF cm^{-2}) or MnO_2 (6 mF cm^{-2}). The relaxation time estimated by the electrochemical impedance spectra was only 4 ns demonstrating the ability for fast delivery of high energy density. The energy and power density were 29-25 mJ cm^{-2} and 0.1-3 mW cm^{-2} at current densities varying in the range of 0.1-2 mA cm^{-2}. The device lifetime was verified over 15,000 charges/discharge cycles performed at 1 mA cm^{-2} within 2.5 V-wide potential windows and the MSC kept 80% of its initial capacitance. These electrical parameters are outstanding among other SiNWs based micro-supercapacitor that highlight enormous potential of PEDOT-D@SiNWs electrodes for energy storage devices.

Gao *et al*. [44] fabricated diamond nanowires (15-20 nm in diameter) via a top-down etching approach [45], which was used further as a substrate for the nickel deposition (20, 40 and 60 nm) by DC sputtering. Anodization of the substrate in 3 M NaOH resulted in NiDia electrode material. According to the SEM analysis illustrated in Figure 16A, the metallic Ni coverage was converted into the porous β-$Ni(OH)_2$ structure stable in alkaline solution with simultaneous wire widening up to *ca*. 50 nm. When the thickness of deposited Ni increases, the nickel hydroxide layer become more corrugated. The CV shape recorded in 3 M NaOH (Figure 16B) shows reversible redox process.

Figure 16

The specific capacitance of a 60 nm-thick Ni coating was 91 mF cm^{-2} at 5 mV s^{-1}. However, the highest gravimetric capacitance of 1601 F g^{-1} was obtained by taking into account only the $Ni(OH)_2$ mass, for NiDia20 sample indicating the presence of non-effective atoms in the active material when the Ni thickness increases too much (hampered diffusion process, lower collection efficiency). The relaxation time, interpreted as the shortest discharging time with an efficiency of 50% [46] rose from 7.15 ms for NiDia20 up to 18.2 ms for NiDia-0. The power density was in the range of 105-106 W kg^{-1} that is one order of magnitude higher and energy density between 10-100 Wh kg^{-1} that is comparable with the currently obtained values. The stability verified by 1000 CV cycles in the potential range of 0.5 V at 100 mV s^{-1} is on the level of 80-70% of the initial capacitance value for the NiDia samples.

Shi *et al*. [47] reported the BDD films grown on Ta plate as a substrate for Ti layer (100 nm) deposition via magnetron sputtering, followed by anodization in fluoride-containing solution. According to the SEM investigations (Figure 17A), the average crystal size of BDD was 30 μm, while the obtained TiO_2 of 80 nm-thickness increased the surface roughness and the number of electroactive sites. The electrochemical performance in a 0.1 M Na_2SO_4 over the potential range of 0-0.9 V shown in Figure 17B presents a higher current density of TiO_2/BDD/Ta material in comparison with BDD/Ta and TiO_2/BDD films. The redox activity arises from the tantalum substrate reaction: $2Ta + 5H \rightarrow Ta_2O_5 + 10H^+ + 10e^-$ and increases significantly the pseudocapacitance, whereas nanostructured titania is responsible for ions absorption enhancing the charge transfer efficiency. The specific capacitance of the composite reaches 5.23 mF cm^{-2} at the scan rate of 5 mV s^{-1} and decreases when the scan rate increases. The GCD curves recorded within 0.9 V potential window at different current densities: 10-160 μA cm^{-2} leads to the specific capacitance of 5.4-0.7 mF cm^{-2}, respectively. After 250 and 500 cycles, the 96.4% and 89.3% retention of the initial capacitance is observed. It should also be noted that fabricated device supplies light-emitting diode for *ca*. 40s after charging at 10 mA cm^{-2}.

Figure 17

Apart from titania, manganese oxide as a part of the diamond-based heterojunction was proposed by Yu *et al*. [48]. The electrode material was obtained by potentiostatic electrodeposition of MnO_2 films with different mass (2-26 μg cm^{-2}) from $MnSO_4$ solution on the BDD, which was grown on Si wafer in trimethyl boron containing atmosphere. The SEM images (Figure 18A) show grain size of BDD to be 0.3-10 μm and thickness of 1.5 μm. While a porous MnO_2 layer is deposited with 24 μg cm^{-2}, it covers BDD completely without any cracks as displayed in Figure 18C.

Figure 18

By both CV and GDC, the specific capacitance of bare BDD was calculated to be 3.6 μF cm^{-2} at the scan rate of 10 mV s^{-1} or current density of 0.05 μA cm^{-2}, respectively. Furthermore, only 5% reduction of the capacitance was observed upon 1000 charge/discharge cycles in comparison with 12% loss for hollow mesoporous shell carbon capsules [49]. For BDD/MnO_2 electrode material, CV shape (Figure 18D) exhibits pseudocapacitive behavior with a pair of broad waves resulting from the redox activity following the reaction.

The highest capacitance reaches 7.9 mF cm^{-2} when MnO_2 was deposited at 24 µg cm^{-2} and decreases for further increase of the oxide amount originating from its poor electrical conductivity and the reduction of the active surface area because of the arising cracks. Taking into account the charge/discharge tests and the mass of deposited manganese oxide, the gravimetric capacitance was calculated to be 349 F g^{-1} at the current density of 3 A g^{-1}, that is much higher than that obtained for graphene (218 F g^{-1} at 5 A g^{-1} [50]), graphene oxide (216 F g^{-1} at 0.15 A g^{-1} [51]), carbon nanospheres (252 F g^{-1} at 2 mV s^{-1} [52]) or nanotubes (201 F g^{-1} at 1 A g^{-1} [53]). After 1000 cycles, a loss of 34% of the initial capacitance can be attributed to: (i) the relatively weak binding between MnO_2 film and BDD substrate, (ii) irreversible redox reaction during charging/discharging process, (iii) fouling of porous BDD/MnO_2 porous structure by impurity molecules and (iv) mechanical expansion of manganese oxide due to the intercalation/deintercalation of electrolyte cations lowering the structure stability. To improve the capacitance retention, the formation of micro- or nanostructured surface of BDD, electrochemical grafting of the linker between diamond and metal oxide as well as surface termination were proposed, but there is no available report on this matter.

Titania nanotubes (TiO_2NT) modified by boron doped diamond is a promising candidate for the fabrication of supercapacitors [14,54,55]. On the contrary to Shi *et al*. [47], the highly ordered layer of titania (8 µm in length and 30 nm in internal diameter) was produced by anodization of Ti metal plate serving as a substrate for the BDD growth (Figure 19A) during the CVD process with different diborane concentration in the gas phase (B/C ratio equals 2000, 5000 and 10000). The Raman spectra differ from the typical one and show the narrow sp^3 band, the wide sp^2 band as well as a signal attributed to the nanocrystalline diamond and CH stretching vibrations. Figure 18B exhibits clear capacitive behavior with significantly higher current densities in comparison with bare titania or BDD. The specific areal capacitance was 7.46, 4.79 and 2.1 mF cm^{-2} for TiO_2 modified with BDD at B/C ratio of 10000, 5000 and 2000, respectively; whereas for pure BDD only 0.11 mF cm^{-2} was reached. The capacitive behavior of the TiO_2NT/BDD material also stands out when CV is recorded in the presence of $[Fe(CN_6)]^{3-/4-}$ redox couple. The active surface area of TiO_2NT/BDD-10k was 1062 cm^2. The detailed studies on the origin of the enhanced electrochemical activity of fabricated titania based diamond composites [14,55] showed that such promising capacitive properties could be attributed to two main factors. First, it concerns specific architecture of TiO_2NT providing high real surface area and straight path for charge percolation, while the second is related to the modification of titania structure induced by BDD coverage during MWPECVD process involving: partial

transformation from anatase to rutile phase, Ti-C bonding that improves integration between titania and BDD part as well as appearance Ti^{3+} affecting sample conductivity.

Figure 19

Summary and Outlook

During the past decade, various types of carbon nanomaterials have been employed for the fabrication of supercapacitors. Although diamond does not seem a suitable choice because of the chemical inactivity of the sp^3 carbon and its high cost, recent studies have shown considerable advantages of diamond-based supercapacitors. Due to the exceptionally low price of novel carbon nanomaterials, which can be easily synthesized from biomass and waste, diamond supercapacitors cannot economically compete with the available supercapacitors, but there is a rare opportunity for designing new types of supercapacitors.

The electrochemical inactivity of diamond is indeed an advantage in the design of diamond supercapacitor, as provides a wide stable potential in which the supercapacitor can operate. Owing to the fact that the energy density of supercapacitor is proportional to the square of the operating voltage, this can be very beneficial for the fabrication of high energy density supercapacitors which can somewhat justify the diamond cost.

It should be taken into account that neither electrochemistry nor materials chemistry of diamond is as advanced as those of graphene and similar carbonaceous nanomaterials. Therefore, the opportunities for the practical development of the diamond supercapacitors is way beyond the available reports. The key point in the design of the diamond supercapacitors is that the internal structure of diamond is electrochemically inaccessible, and thus, the size of diamond nanoparticles should be minimized to enhance the supercapacitor performance. Hypothetically, if reducing the particle size to that of a single unit cell, the supercapacitor behavior of diamond will be maximized. In fact, the ratio of the internal sp^2 carbon atoms to the external dangling bonds should be reduced.

Acknowledgements

The authors gratefully acknowledge financial support from the Polish National Science Centre (NCN) under Grant No. 2012/07/D/ST5/02269, 2015/17/D/ST5/02571 and 2014/14/M/ST5/00715. The DS funds of the Faculty of Electronics, Telecommunications and Informatics of the Gdansk University of Technology are also acknowledged. K.S. research was supported by the Foundation for Polish Science (FNP).

Figures

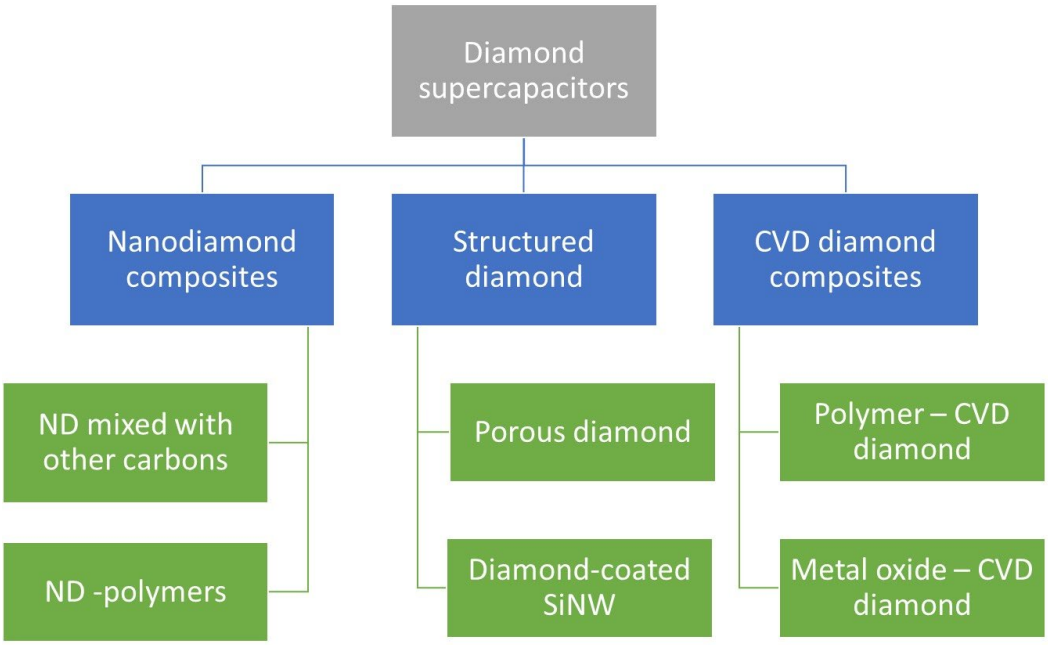

Figure 1. Classification of diamond-based electrode materials used for capacitors and energy storage devices.

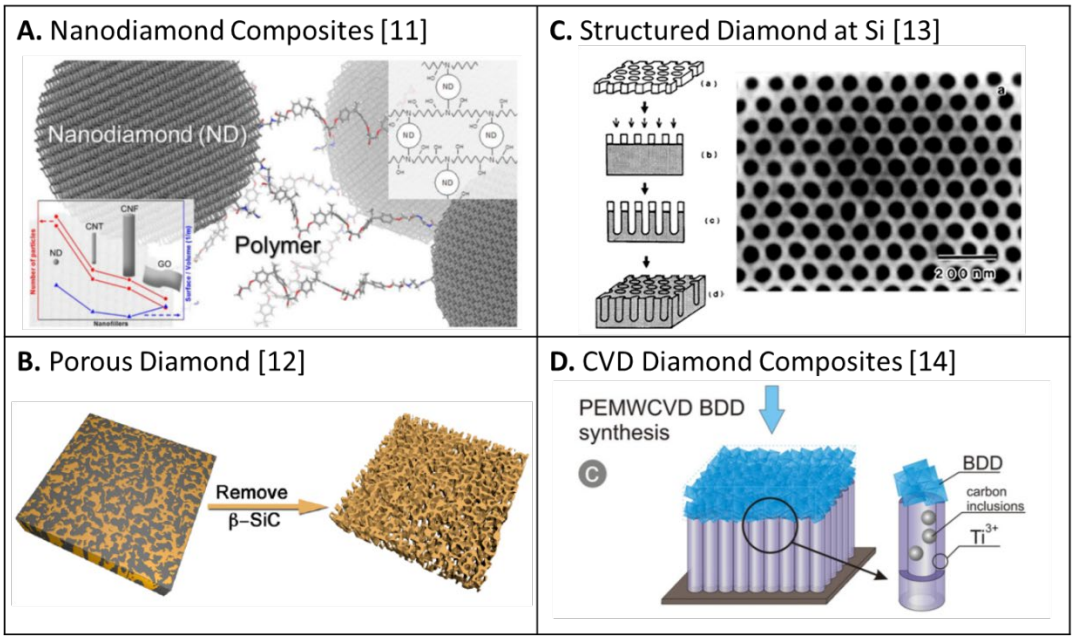

Figure 2. Methods of area surface development of CVD grown diamond and nanodiamond applied for energy storage devices. Reproduced with permission from Ref. [11–14]. Copyright 2015, Elsevier, MPDI, The Electrochemical Society and American Chemical Society.

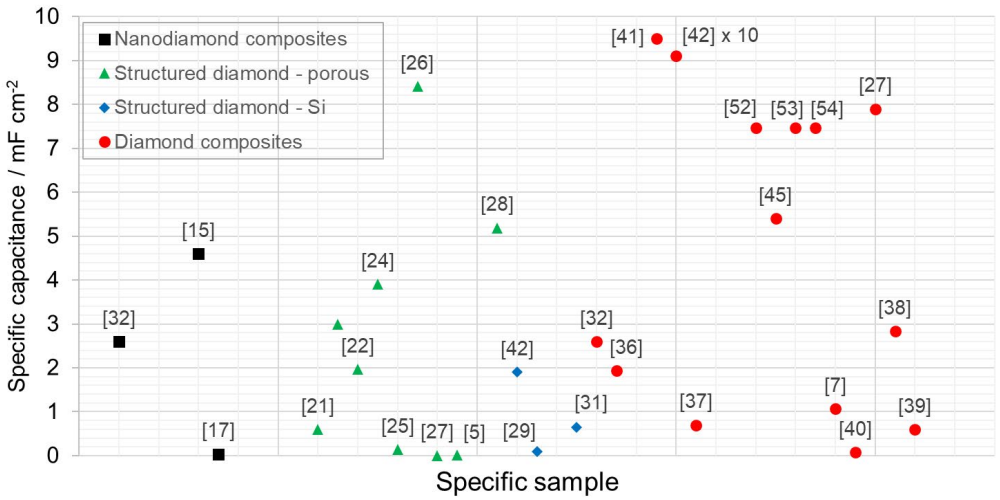

Figure 3. Classification of diamond based energy storage devices resulting from specific surface nanostructuring approaches.

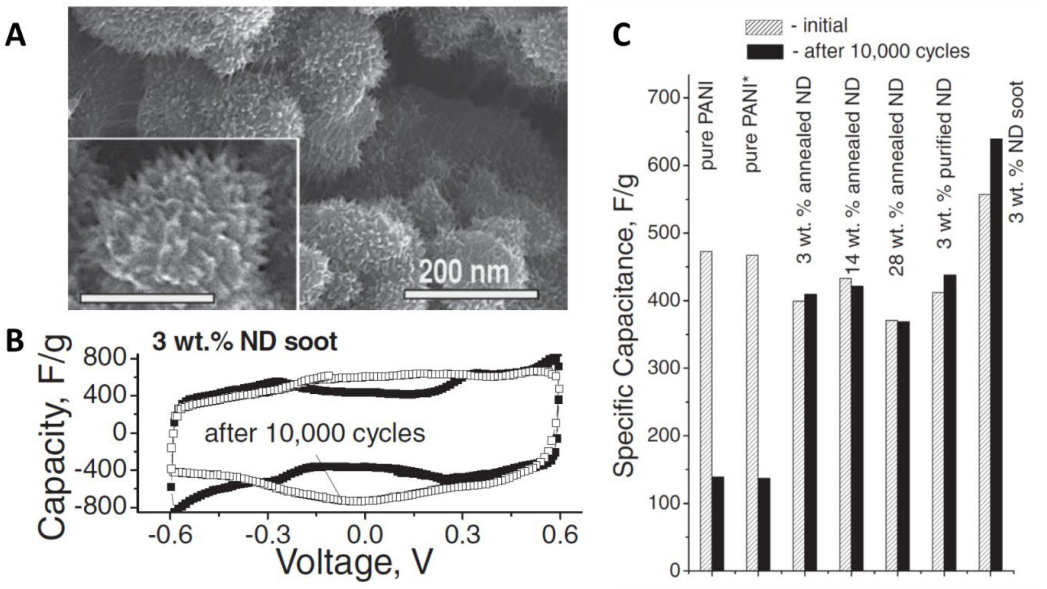

Figure 4. Enhanced capacity of nanodiamond-polymer composites: (A) Micro-image of nanodiamond-polyaniline composite surface, (B) Cyclic voltammetry of PANI with embedded 3 wt.% ND soot, (C) Integrated average specific capacitance of the DND-PANI electrodes before and after 10 000 cycles. Reproduced with permission from Ref. [16]. Copyright 2010, Wiley-VCH.

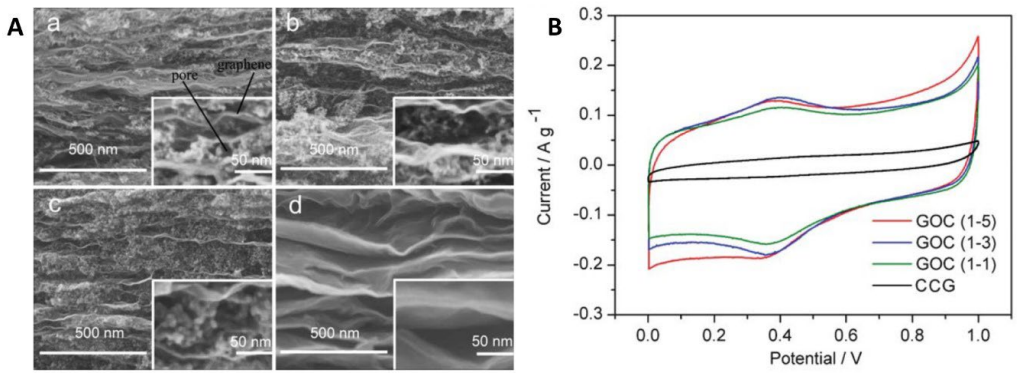

Figure 5. The SEM cross-section images of the graphene-OLC (GOC) composite films with thicknesses prepared with the mixtures of GO and OLC with weight ratios of 1:1, 1:3 and 1:5 (attn. GOC(1–1), GOC(1–3), GOC(1–5)) (A); Cyclic voltammograms of a chemically converted graphene film and GOC composite films with different mixtures ratio studied in 1 M H_2SO_4 aqueous solution. (B) Reproduced with permission from Ref. [20]. Copyright 2011, Royal Society of Chemistry.

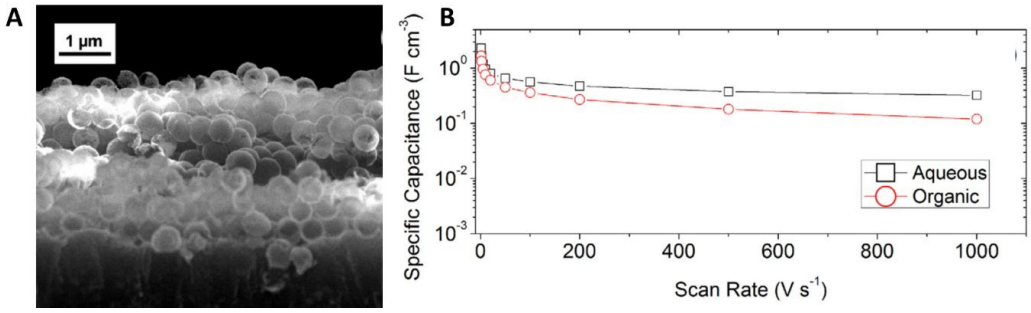

Figure 6. The cross-section SEM of boron-doped diamond foam (A); Volumetric capacitance of diamond foam *vs*. scan rate (B) Reproduced with permission from Ref. [24]. Copyright 2014, Elsevier.

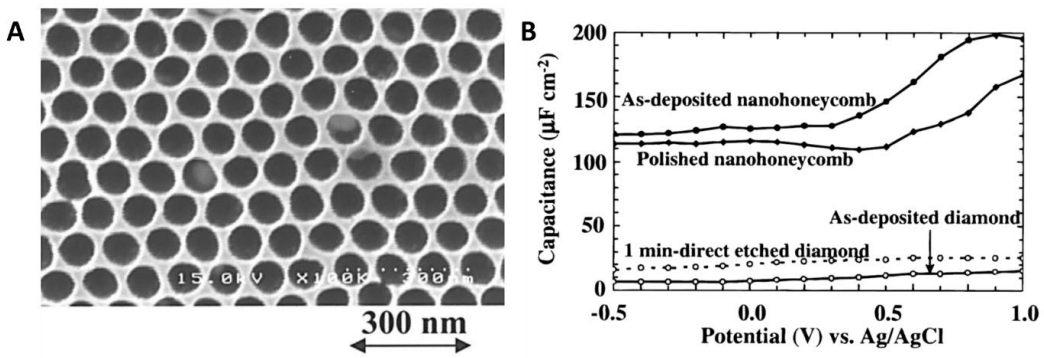

Figure 7. The top-view SEM of a highly boron-doped nano-honeycomb diamond electrode (A); Potential dependence of capacitance for planar and various etched diamond electrodes investigated in 0.1 M H_2SO_4 electrolyte (B) Reproduced with permission from Ref. [26,27]. Copyright 2000, The Electrochemical Society.

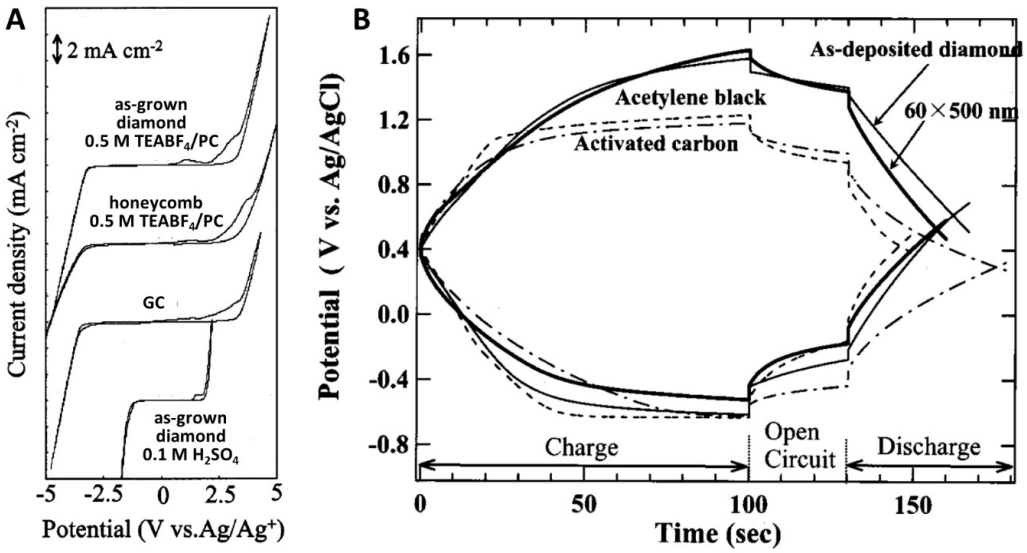

Figure 8. The cyclic voltammograms obtained for various boron-doped electrodes. Glassy carbon (GC) was displayed for comparison (A). Charge-discharge behavior of as-deposited diamond (solid line), honeycomb diamond (thick solid line), acetylene black (dotted line), and activated carbon (dot-dashed line) recorded in 1 M H_2SO_4 (B) Reproduced with permission from Ref. [5] and [27] . Copyright 2001, Elsevier and The Electrochemical Society.

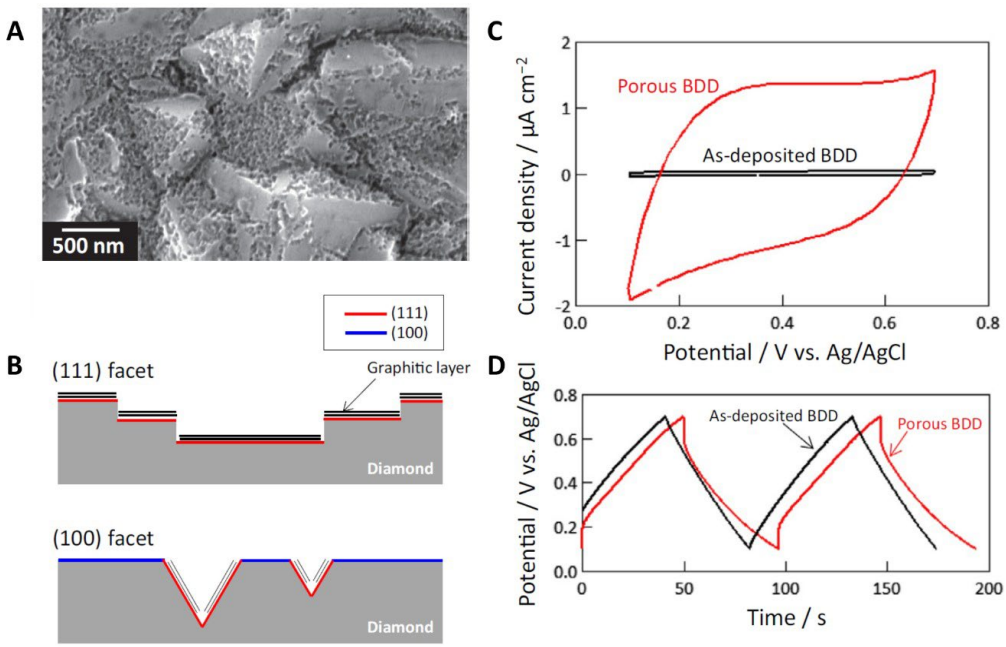

Figure 9. The SEM image of graphitized porous boron doped diamond (BDD) (A); the mechanism of diamond surface etching via graphitization on (111) and (100) facets (B); CV curves for as-deposited and porous BDD electrodes (C); Galvanostatic charge–discharge curves both measured in 1 M Na_2SO_4 (D) Reproduced with permission from Ref. [28]. Copyright 2014, Elsevier.

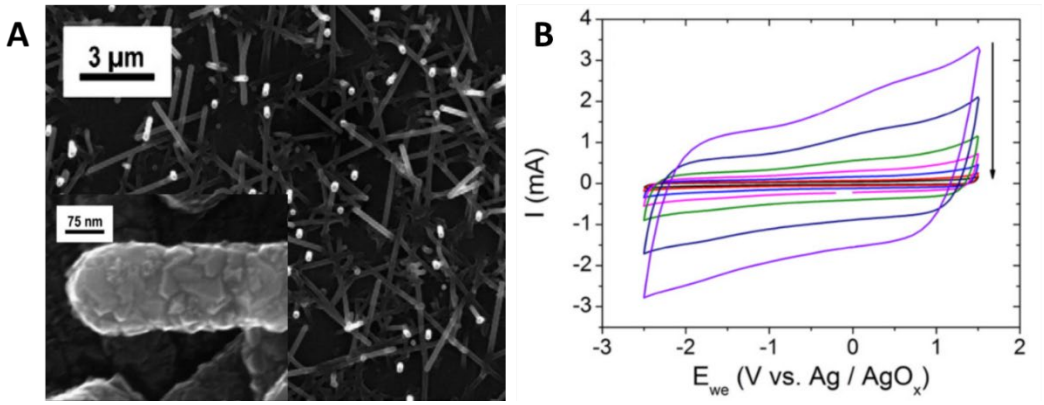

Figure 10. SEM images of diamond-coated silicon wire sample, and a large scale picture of the same sample showing the density and uniformity (A); CV curves at 1, 2, 5, 10, 20, 50, and 100 V/s between -2.5 and +1.5 V in 40 vol.% PMPyrrTFSI in PC, scan rates decrease along the direction of the arrow (B) Reproduced with permission from Ref. [31]. Copyright 2015, Elsevier.

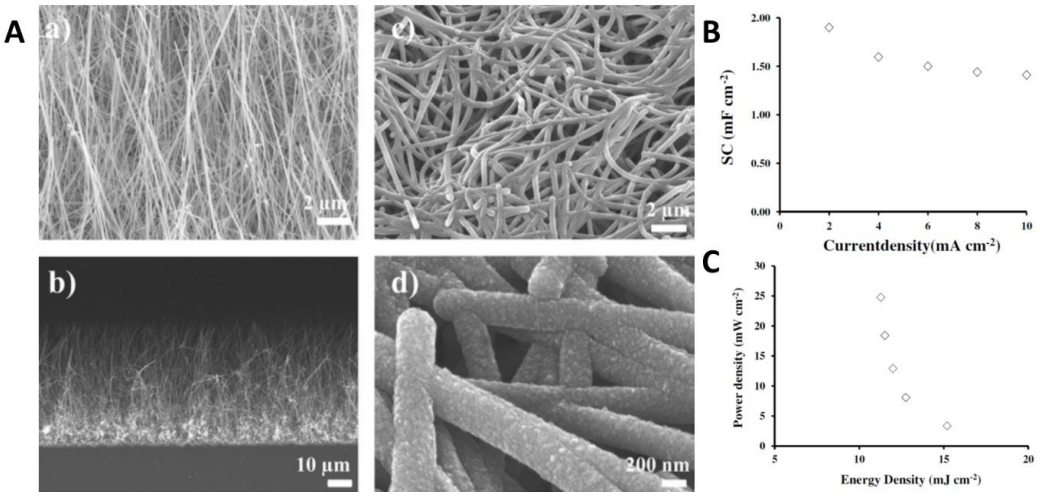

Figure 11. SEM image of the morphology of SiNWs recorded at 45° tilted angle. b) Cross-sectional view of SiNWs. c) and d) Low and high resolution SEM images of diamond coated SiNWs (A); Specific capacitance versus current density (B) and Ragone plot at different current densities (C) Reproduced with permission from Ref. [32]. Copyright 2016, Elsevier.

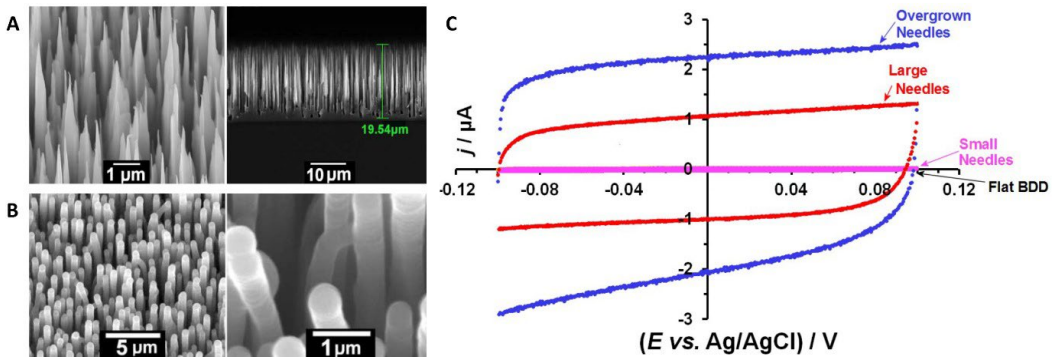

Figure 12. SEM images of two types of black Si before coating with diamond, long needles with length 15–20 mm (A); Long black Si needles coated with boron-doped MCD (B); Cyclic voltammograms recorded only in presence of background electrolyte solution (KNO_3) for 4 types of diamond electrode deposited (C) Reproduced with permission from Ref. [33]. Copyright 2016, Royal Society of Chemistry.

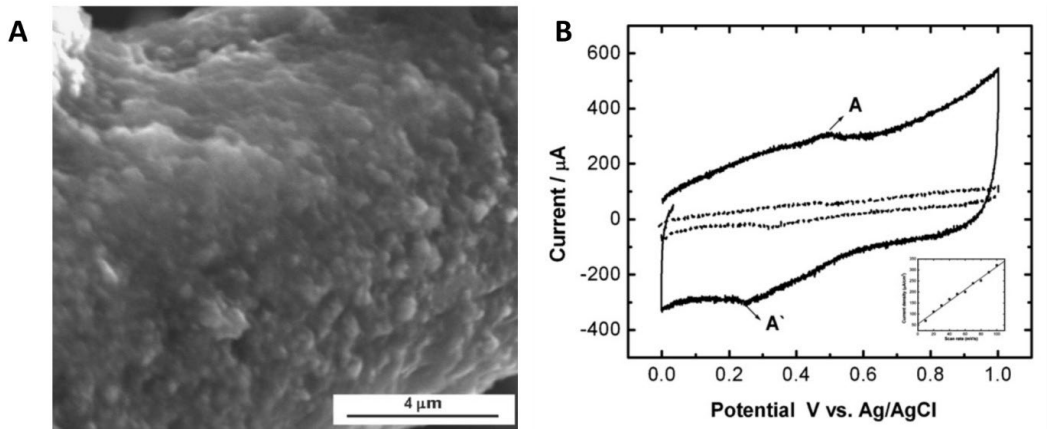

Figure 13. SEM image of NCD grown on carbon fiber treated at temperature of 1300 K (A); Cyclic voltammograms of NCD/CF-1300 in 0.5 M H_2SO_4 at 100 mV s^{-1} (solid line) and 10 mV s^{-1} (dash line) (B) Reproduced with permission from Ref. [34]. Copyright 2007, Elsevier.

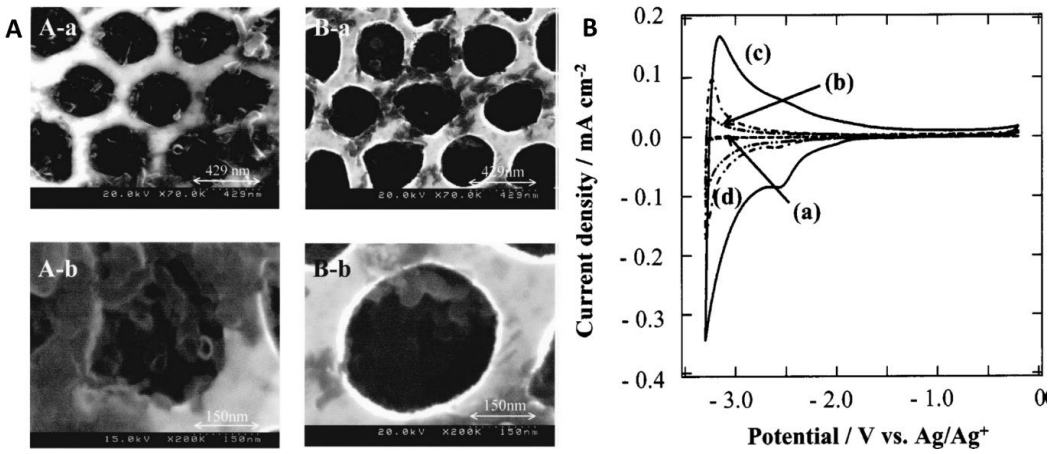

Figure 14. Top view of SEM images for a carbon nanotubes/nanoporous diamond composite electrode. Low magnification and high magnification images for HD CNT-NANO and LD CNT-NANO (A); Cyclic voltammograms for: a) as-deposited diamond, b) CNTAD, c) HD CNT-NANO, and d) LD CNT-NANO electrodes in 1 M $LiClO_4$/PC. Sweep rate: 0.3 mV s^{-1}; geometric area: 0.03 cm^2 (B) Reproduced with permission from Ref. [39]. Copyright 2004, The Electrochemical Society.

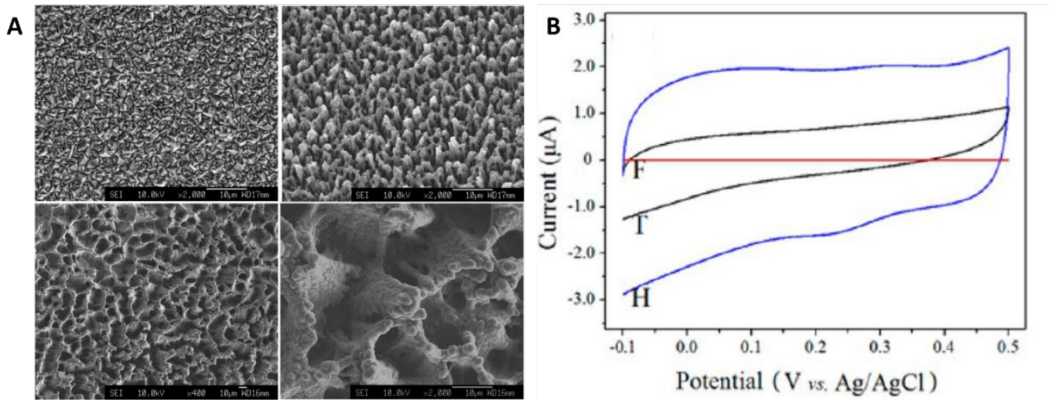

Figure 15. Electron micrograph images of the three types of BDD electrode under study: (a) microcrystalline flat diamond film, (b) CNT/BDD teepee matrix, (c) CNT/BDD ridged/honeycomb surface, and (d) higher magnification view of the film in (c) (A); Comparison of cyclic voltammetry curves of 0.1 M KNO_3 for the three types of BDD electrodes (flat (F), teepee (T), and honeycomb (H)), all taken at a constant 10 mV/s scan rate (B). Reproduced with permission from Ref. [40]. Copyright 2014, American Chemical Society.

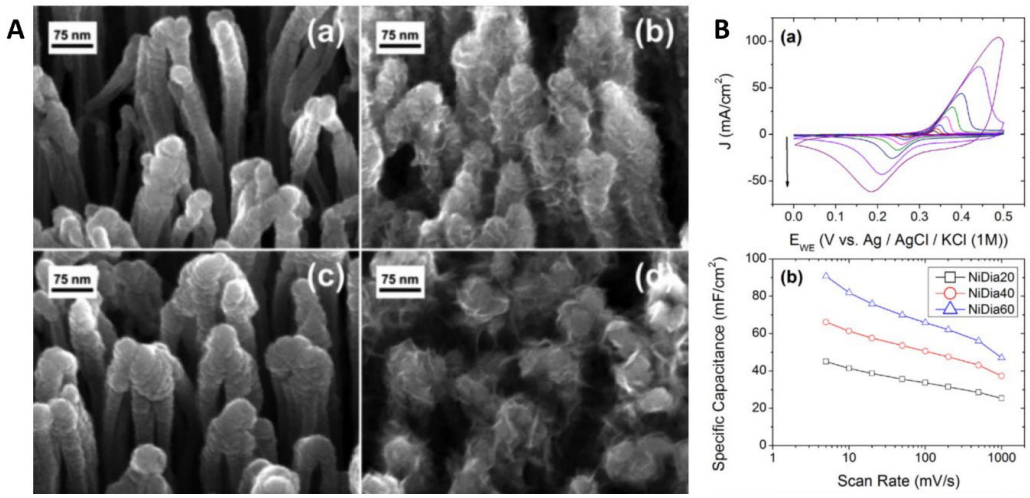

Figure 16. SEM images of NiDia40 (a, b) and NiDia60 (c, d) before (a, c) and after (b, d) anodization effective surface area (A); Cyclic voltammetry (a) of a NiDia20 sample between 0 and 0.5V at 5, 10, 20, 50, 100, 200, 500, and 1000 mV s^{-1} (scan rates increase along the arrow direction), (b) areal, vs scan rate of different samples (B) Reproduced with permission from Ref. [44]. Copyright 2015, Wiley-VCH.

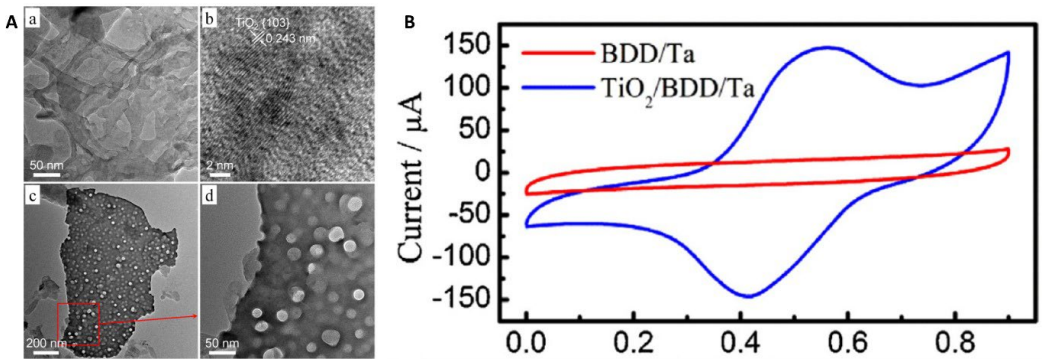

Figure 17. (a) TEM and (b) high-resolution TEM images of TiO_2 layer, and TEM images of Ta layer at (c) low magnification and (d) high magnification (A); Cyclic voltammograms of BDD/Ta and TiO_2/BDD/Ta multilayer films at scan rate of 50 mV s^{-1} (B) Reproduced with permission from Ref. [47]. Copyright 2015, Elsevier.

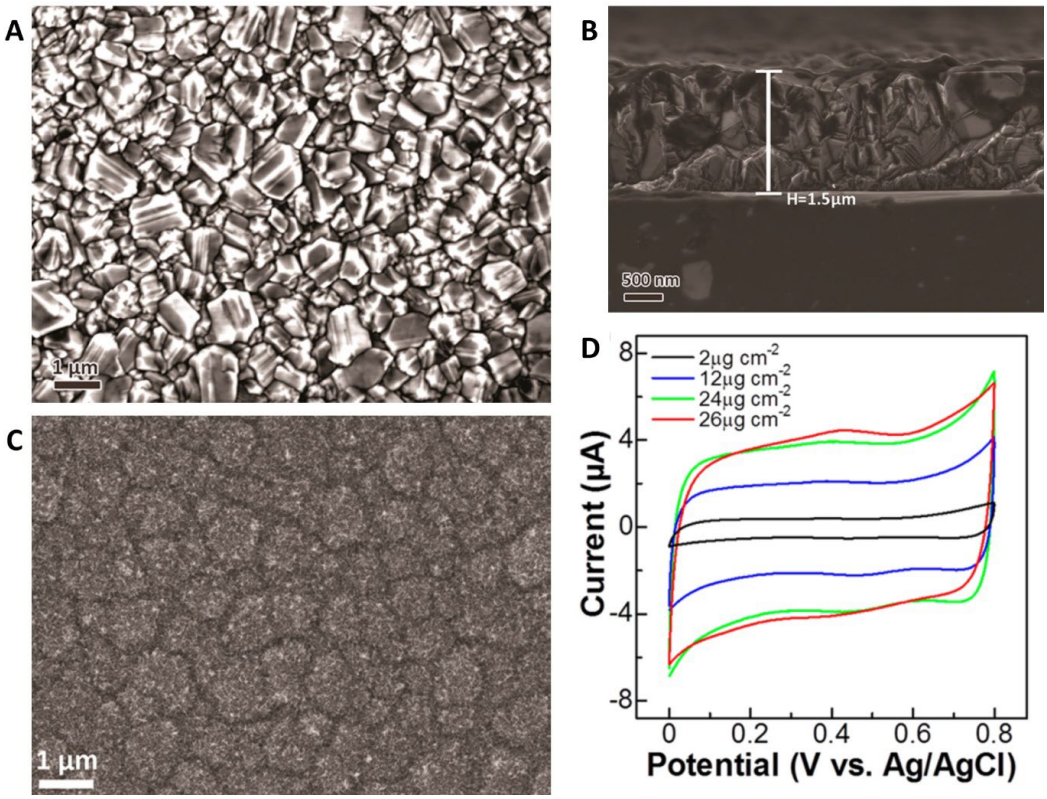

Figure 18. SEM of BDD samples: top view (A); side view (B); a top view SEM images of MnO_2 films coated on diamond with area densities of 24 µg cm^{-2} (C); Cyclic voltammograms of MnO_2 film-coated BDD electrode with area densities of 2.0, 12, 24, and 26 µg cm^{-2} (D) Reproduced with permission from Ref. [48]. Copyright 2015, American Chemical Society.

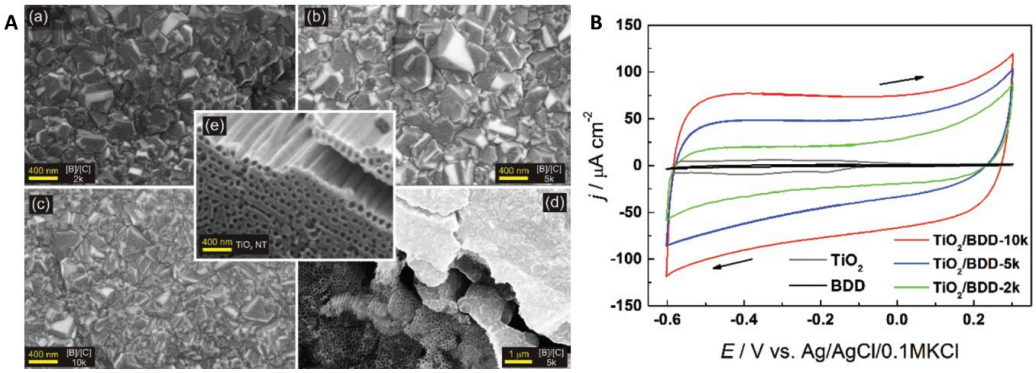

Figure 19. SEM images of the electrode surface recorded for samples with the B/C ratio of (a) 2000, (b) 5000, and (c) 10 000, and (e) a freshly anodized TiO_2 nanotube array. In (d), the diamond layer is partially removed from the surface and the unaffected TiO_2 nanotube structure can be observed (A); Cyclic voltammetry curves registered for the composite electrodes TiO_2/BDD with different B/C ratios and, as the reference, for pure titania and BDD layers immersed in 0.1 M $NaNO_3$ (10 mV s^{-1}) (B) Reproduced with permission from Ref. [54]. Copyright 2015, Royal Society of Chemistry.

Figure Captions

Figure 1. Classification of diamond-based electrode materials used for capacitors and energy storage devices.

Figure 2. Methods of area surface development of CVD grown diamond and nanodiamond applied for energy storage devices. Reproduced with permission from Ref. [10–13]. Copyright 2015, Elsevier, MPDI, The Electrochemical Society and American Chemical Society.

Figure 3. Classification of diamond based energy storage devices resulting from specific surface nanostructuring approaches.

Figure 4. Enhanced capacity of nanodiamond-polymer composites: (A) Micro-image of nanodiamond-polyaniline composite surface, (B) Cyclic voltammetry of PANI with embedded 3 wt.% ND soot, (C) Integrated average specific capacitance of the DND-PANI electrodes before and after 10 000 cycles. Reproduced with permission from Ref. [14]. Copyright 2010, Wiley-VCH.

Figure 5. The SEM cross-section images of the graphene-OLC (GOC) composite films with thicknesses prepared with the mixtures of GO and OLC with weight ratios of 1:1, 1:3 and 1:5 (attn. GOC(1–1), GOC(1–3), GOC(1–5)) (A); Cyclic voltammograms of a chemically converted graphene film and GOC composite films with different mixtures ratio studied in 1 M H_2SO_4 aqueous solution. (B) Reproduced with permission from Ref. [21]. Copyright 2011, Royal Society of Chemistry.

Figure 6. The cross-section SEM of boron-doped diamond foam (A); Volumetric capacitance of diamond foam *vs*. scan rate (B) Reproduced with permission from Ref. [25]. Copyright 2014, Elsevier.

Figure 7. The top-view SEM of a highly boron-doped nano-honeycomb diamond electrode (A); Potential dependence of capacitance for planar and various etched diamond electrodes investigated in 0.1 M H_2SO_4 electrolyte (B) Reproduced with permission from Ref. [27,28]. Copyright 2000, The Electrochemical Society.

Figure 8. The cyclic voltammograms obtained for various boron-doped electrodes. Glassy carbon (GC) was displayed for comparison (A). Charge-discharge behavior of as-deposited diamond (solid line), honeycomb diamond (thick solid line), acetylene black (dotted line), and activated carbon (dot-dashed line) recorded in 1 M H_2SO_4 (B) Reproduced with permission from Ref. [5] and [28] . Copyright 2001, Elsevier and The Electrochemical Society.

Figure 9. The SEM image of graphitized porous boron doped diamond (BDD) (A); the mechanism of diamond surface etching via graphitization on (111) and (100) facets (B); CV curves for as-deposited and porous BDD electrodes (C); Galvanostatic charge–discharge curves both measured in 1 M Na_2SO_4 (D) Reproduced with permission from Ref. [29]. Copyright 2014, Elsevier.

Figure 10. SEM images of diamond-coated silicon wire sample, and a large scale picture of the same sample showing the density and uniformity (A); CV curves at 1, 2, 5, 10, 20, 50, and 100 V/s between -2.5 and +1.5 V in 40 vol.% PMPyrrTFSI in PC, scan rates decrease along the direction of the arrow (B) Reproduced with permission from Ref. [32]. Copyright 2015, Elsevier.

Figure 11. SEM image of the morphology of SiNWs recorded at 45° tilted angle. b) Cross-sectional view of SiNWs. c) and d) Low and high resolution SEM images of diamond coated SiNWs (A); Specific capacitance versus current density (B) and Ragone plot at different current densities (C) Reproduced with permission from Ref. [33]. Copyright 2016, Elsevier.

Figure 12. SEM images of two types of black Si before coating with diamond, long needles with length 15–20 mm (A); Long black Si needles coated with boron-doped MCD (B); Cyclic voltammograms recorded only in presence of background electrolyte solution (KNO_3) for 4 types of diamond electrode deposited (C) Reproduced with permission from Ref. [34]. Copyright 2016, Royal Society of Chemistry.

Figure 13. SEM image of NCD grown on carbon fiber treated at temperature of 1300 K (A); Cyclic voltammograms of NCD/CF-1300 in 0.5 M H_2SO_4 at 100 mV s^{-1} (solid line) and 10 mV s^{-1} (dash line) (B) Reproduced with permission from Ref. [35]. Copyright 2007, Elsevier.

Figure 14. Top view of SEM images for a carbon nanotubes/nanoporous diamond composite electrode. Low magnification and high magnification images for HD CNT-NANO and LD CNT-NANO (A); Cyclic voltammograms for: a) as-deposited diamond, b) CNTAD, c) HD CNT-NANO, and d) LD CNT-NANO electrodes in 1 M $LiClO_4$/PC. Sweep rate: 0.3 mV s^{-1}; geometric area: 0.03 cm^2 (B) Reproduced with permission from Ref. [40]. Copyright 2004, The Electrochemical Society.

Figure 15. Electron micrograph images of the three types of BDD electrode under study: (a) microcrystalline flat diamond film, (b) CNT/BDD teepee matrix, (c) CNT/BDD ridged/honeycomb surface, and (d) higher magnification view of the film in (c) (A); Comparison of cyclic voltammetry curves of 0.1 M KNO3 for the three types of BDD electrodes (flat (F), teepee (T), and honeycomb (H)), all taken at a constant 10 mV/s scan rate (B). Reproduced with permission from Ref. [41].

Copyright 2014, American Chemical Society.

Figure 16. SEM images of NiDia40 (a, b) and NiDia60 (c, d) before (a, c) and after (b, d) anodization effective surface area (A); Cyclic voltammetry (a) of a NiDia20 sample between 0 and 0.5V at 5, 10, 20, 50, 100, 200, 500, and 1000 mV s^{-1} (scan rates increase along the arrow direction), (b) areal, vs scan rate of different samples (B) Reproduced with permission from Ref. [45]. Copyright 2015, Wiley-VCH.

Figure 17. (a) TEM and (b) high-resolution TEM images of TiO_2 layer, and TEM images of Ta layer at (c) low magnification and (d) high magnification (A); Cyclic voltammograms of BDD/Ta and TiO_2/BDD/Ta multilayer films at scan rate of 50 mV s^{-1} (B) Reproduced with permission from Ref. [48]. Copyright 2015, Elsevier.

Figure 18. SEM of BDD samples: top view (A); side view (B); a top view SEM images of MnO_2 films coated on diamond with area densities of 24 μg cm^{-2} (C); Cyclic voltammograms of MnO_2 film-coated BDD electrode with area densities of 2.0, 12, 24, and 26 μg cm^{-2} (D) Reproduced with permission from Ref. [49]. Copyright 2015, American Chemical Society.

Figure 19. SEM images of the electrode surface recorded for samples with the B/C ratio of (a) 2000, (b) 5000, and (c) 10 000, and (e) a freshly anodized TiO_2 nanotube array. In (d), the diamond layer is partially removed from the surface and the unaffected TiO_2 nanotube structure can be observed (A); Cyclic voltammetry curves registered for the composite electrodes TiO_2/BDD with different B/C ratios and, as the reference, for pure titania and BDD layers immersed in 0.1 M $NaNO_3$ (10 mV s^{-1}) (B) Reproduced with permission from Ref. [55]. Copyright 2015, Royal Society of Chemistry.

References

[1] A. G. Pandolfo, A. F. Hollenkamp, *J. Power Sources* **2006**, *157*, 11–27.
[2] P. Simon, Y. Gogotsi, *Nat. Mater.* **2008**, *7*, 845–854.
[3] A. Eftekhari, *Microporous Mesoporous Mater.* **2017**, *243*, 355–369.
[4] R. Ramesham, P. E. Pehrsson, T. I. Smith, M. F. Rose, *J. Mater. Sci. Mater. Electron.* **1997**, *8*, 69–72.
[5] M. Yoshimura, K. Honda, R. Uchikado, T. Kondo, T. N. Rao, D. A. Tryk, A. Fujishima, Y. Sakamoto, K. Yasui, H. Masuda, *Diam. Relat. Mater.* **2001**, *10*, 620–626.
[6] W. Ebert, M. Adamschik, P. Gluche, A. Flöter, E. Kohn, *Diam. Relat. Mater.* **1999**, *8*, 1875–1877.
[7] W. Tong, K. Fox, A. Zamani, A. M. Turnley, K. Ganesan, A. Ahnood, R. Cicione, H. Meffin, S. Prawer, A. Stacey, et al., *Biomaterials* **2016**, *104*, 32–42.
[8] F. Gao, C. E. Nebel, *ACS Appl. Mater. Interfaces* **2016**, *8*, 28244–28254.
[9] N. Yang, J. S. Foord, X. Jiang, *Carbon* **2016**, *99*, 90–110.
[10] A. Eftekhari, H. Garcia, *Mater. Today Chem.* **2017**, *4*, 1–16.
[11] V. N. Mochalin, Y. Gogotsi, *Diam. Relat. Mater.* **2015**, *58*, 161–171.
[12] S. Szunerits, Y. Coffinier, R. Boukherroub, *Sensors* **2015**, *15*, 12573–12593.
[13] H. Zhuang, N. Yang, H. Fu, L. Zhang, C. Wang, N. Huang, X. Jiang, *ACS Appl. Mater. Interfaces* **2015**, *7*, 5384–5390.
[14] M. Sawczak, M. Sobaszek, K. Siuzdak, J. Ryl, R. Bogdanowicz, K. Darowicki, M. Gazda, A. Cenian, *J. Electrochem. Soc.* **2015**, *162*, A2085–A2092.
[15] A. Eftekhari, L. Li, Y. Yang, *J. Power Sources* **2017**, *347*, 86–107.
[16] I. Kovalenko, D. G. Bucknall, G. Yushin, *Adv. Funct. Mater.* **2010**, *20*, 3979–3986.
[17] J. Zang, Y. Wang, X. Zhao, G. Xin, S. Sun, X. Qu, S. Ren, others, *Int J Electrochem Sci* **2012**, *7*, 1677–1687.
[18] S. Park, K. Lian, Y. Gogotsi, *J. Electrochem. Soc.* **2009**, *156*, A921–A926.
[19] C. Portet, G. Yushin, Y. Gogotsi, *Carbon* **2007**, *45*, 2511–2518.
[20] Y. Sun, Q. Wu, Y. Xu, H. Bai, C. Li, G. Shi, *J. Mater. Chem.* **2011**, *21*, 7154–7160.
[21] Q. Wang, N. Plylahan, M. V. Shelke, R. R. Devarapalli, M. Li, P. Subramanian, T. Djenizian, R. Boukherroub, S. Szunerits, *Carbon* **2014**, *68*, 175–184.
[22] X. X. Zhang, J. X. Wen, R. Fan, D. J. Jiang, X. L. Lou, C. H. Li, G. N. Du, *Mater. Sci. Forum* **2016**, *852*, 939–942.
[23] H. J. Fecht, K. Brühne, *Carbon-Based Nanomaterials and Hybrids: Synthesis, Properties, and Commercial Applications*, CRC Press, **2014**.
[24] F. Gao, M. T. Wolfer, C. E. Nebel, *Carbon* **2014**, *80*, 833–840.
[25] C. Hébert, E. Scorsone, M. Mermoux, P. Bergonzo, *Carbon* **2015**, *90*, 102–109.
[26] K. Honda, T. N. Rao, D. A. Tryk, A. Fujishima, M. Watanabe, K. Yasui, H. Masuda, *J. Electrochem. Soc.* **2000**, *147*, 659–664.
[27] K. Honda, T. N. Rao, D. A. Tryk, A. Fujishima, M. Watanabe, K. Yasui, H. Masuda, *J. Electrochem. Soc.* **2001**, *148*, A668–A679.
[28] T. Kondo, Y. Kodama, S. Ikezoe, K. Yajima, T. Aikawa, M. Yuasa, *Carbon* **2014**, *77*, 783–789.
[29] C. Shi, C. Li, M. Li, H. Li, W. Dai, Y. Wu, B. Yang, *Appl. Surf. Sci.* **2016**, *360*, *Part A*, 315–322.
[30] V. D. van Wyk, P. G. L. Baker, T. Waryo, E. I. Iwuoha, C. O'Sullivan, *Anal. Lett.* **2011**, *44*, 2005–2018.
[31] F. Gao, G. Lewes-Malandrakis, M. T. Wolfer, W. Müller-Sebert, P. Gentile, D. Aradilla, T. Schubert, C. E. Nebel, *Diam. Relat. Mater.* **2015**, *51*, 1–6.
[32] D. Aradilla, F. Gao, G. Lewes-Malandrakis, W. Müller-Sebert, D. Gaboriau, P. Gentile, B.

Iliev, T. Schubert, S. Sadki, G. Bidan, et al., *Electrochem. Commun.* **2016**, *63*, 34–38.
[33] P. W. May, M. Clegg, T. A. Silva, H. Zanin, O. Fatibello-Filho, V. Celorrio, D. J. Fermin, C. C. Welch, G. Hazell, L. Fisher, et al., *J. Mater. Chem. B* **2016**, *4*, 5737–5746.
[34] E. C. Almeida, A. F. Azevedo, M. R. Baldan, N. A. Braga, J. M. Rosolen, N. G. Ferreira, *Chem. Phys. Lett.* **2007**, *438*, 47–52.
[35] E. C. Almeida, A. V. Diniz, J. M. Rosolen, V. J. Trava-Airoldi, N. G. Ferreira, *Diam. Relat. Mater.* **2005**, *14*, 679–684.
[36] E. C. Almeida, A. V. Diniz, V. J. Trava-Airoldi, N. G. Ferreira, *Thin Solid Films* **2005**, *485*, 241–246.
[37] E. C. Almeida, V. J. Trava-Airoldi, M. R. Baldan, J. M. Rosolen, N. G. Ferreira, *J. Mater. Sci.* **2007**, *42*, 2250–2254.
[38] E. C. Almeida, M. R. Baldan, J. M. Rosolen, N. G. Ferreira, *Diam. Relat. Mater.* **2008**, *17*, 1529–1533.
[39] K. Honda, M. Yoshimura, K. Kawakita, A. Fujishima, Y. Sakamoto, K. Yasui, N. Nishio, H. Masuda, *J. Electrochem. Soc.* **2004**, *151*, A532–A541.
[40] H. Zanin, P. W. May, D. J. Fermin, D. Plana, S. M. C. Vieira, W. I. Milne, E. J. Corat, *ACS Appl. Mater. Interfaces* **2014**, *6*, 990–995.
[41] H. Zanin, P. W. May, R. L. Harniman, T. Risbridger, E. J. Corat, D. J. Fermin, *Carbon* **2015**, *82*, 288–296.
[42] X. Tong, M. Liu, G. Zhao, *J. Solid State Electrochem.* **2009**, *14*, 221.
[43] D. Aradilla, F. Gao, G. Lewes-Malandrakis, W. Müller-Sebert, P. Gentile, M. Boniface, D. Aldakov, B. Iliev, T. J. S. Schubert, C. E. Nebel, et al., *ACS Appl. Mater. Interfaces* **2016**, *8*, 18069–18077.
[44] F. Gao, C. E. Nebel, *Phys. Status Solidi A* **2015**, *212*, 2533–2538.
[45] W. Smirnov, A. Kriele, N. Yang, C. E. Nebel, *Diam. Relat. Mater.* **2010**, *19*, 186–189.
[46] P. L. Taberna, P. Simon, J. F. Fauvarque, *J. Electrochem. Soc.* **2003**, *150*, A292–A300.
[47] C. Shi, H. Li, C. Li, M. Li, C. Qu, B. Yang, *Appl. Surf. Sci.* **2015**, *357*, *Part B*, 1380–1387.
[48] S. Yu, N. Yang, H. Zhuang, J. Meyer, S. Mandal, O. A. Williams, I. Lilge, H. Schönherr, X. Jiang, *J. Phys. Chem. C* **2015**, *119*, 18918–18926.
[49] D. Bhattacharjya, M.-S. Kim, T.-S. Bae, J.-S. Yu, *J. Power Sources* **2013**, *244*, 799–805.
[50] S. Deng, D. Sun, C. Wu, H. Wang, J. Liu, Y. Sun, H. Yan, *Electrochimica Acta* **2013**, *111*, 707–712.
[51] S. Chen, J. Zhu, X. Wu, Q. Han, X. Wang, *ACS Nano* **2010**, *4*, 2822–2830.
[52] Y. Zhao, Y. Meng, P. Jiang, *J. Power Sources* **2014**, *259*, 219–226.
[53] L. Li, Z. A. Hu, N. An, Y. Y. Yang, Z. M. Li, H. Y. Wu, *J. Phys. Chem. C* **2014**, *118*, 22865–22872.
[54] K. Siuzdak, R. Bogdanowicz, M. Sawczak, M. Sobaszek, *Nanoscale* **2014**, *7*, 551–558.
[55] M. Sobaszek, K. Siuzdak, M. Sawczak, J. Ryl, R. Bogdanowicz, *Thin Solid Films* **2016**, *601*, 35–40.